AGU PUBLICATIONS

JGR

Journal of Geophysical Research: Atmospheres

RESEARCH ARTICLE

10.1002/2016JD025505

Key Points:

- This study is to use space-based hyperspectral infrared instrument CrIS for detecting optically thin and thick clouds
- Cloud emission and scattering index (CESI) is developed to detect clouds based on different responses of SW and LW CO_2 bands to ice clouds
- The CrIS CESI is unique for detecting optically thin cirrus clouds and can be used for monitoring horizontal and vertical cloud structures

Correspondence to:
X. Zou,
xzou1@umd.edu

Citation:
Lin, L., X. Zou, and F. Weng (2017), Combining CrIS double CO_2 bands for detecting clouds located in different layers of the atmosphere, *J. Geophys. Res. Atmos.*, *122*, 1811–1827, doi:10.1002/2016JD025505.

Received 12 JUN 2016
Accepted 30 JAN 2017
Accepted article online 1 FEB 2017
Published online 10 FEB 2017

Combining CrIS double CO_2 bands for detecting clouds located in different layers of the atmosphere

Lin Lin[1], **Xiaolei Zou**[2], **and Fuzhong Weng**[3]

[1]I. M. Systems Group, Inc., Rockville, Maryland, USA, [2]ESSIC, University of Maryland, College Park, Maryland, USA, [3]Center for Satellite Applications and Research, NOAA, College Park, Maryland, USA

Abstract Detection of clouds within certain vertical layers of the atmosphere from satellite infrared instruments is challenging, especially of those optically thin clouds due to their small thermal contrasts to the background. This study develops a new method for cloud detection by using the Cross-track Infrared Sounder (CrIS) hyperspectral radiances at shortwave (~4.3 μm) and longwave (~15 μm) CO_2 bands. Specifically, CrIS longwave channels are first paired with shortwave channels based on weighting function altitudes and sensitivity to clouds. A linear relationship of brightness temperatures between each paired channel is then derived for predicting the shortwave channel from the longwave channel in clear-sky conditions. A cloud emission and scattering index (CESI) can finally be defined as the difference of the paired shortwave channel between the clear-sky, regression model predicted and the observed brightness temperatures. Spatial distributions of such derived CESI for several paired channels in the troposphere are examined for a winter storm that occurred in the eastern part of the United States during 22–24 January 2016. It is shown that the CESI values over the storm regions with optically thin cirrus, fog, and supercooled water clouds are positively larger than those over optically thick opaque ice and overshooting clouds or in clear-sky conditions. Of particular interest is that an area of fog and water clouds over Gulf of Mexico, which are indicated by the Visible Infrared Imaging Radiometer Suite day and night band observations, is identified by the CESI. The global distribution of CESIs derived from CrIS double CO_2 bands with weighting functions peak around 321 hPa agrees well with the distribution of ice cloud optical thickness from the Atmospheric Infrared Sounder version 6 cloud product data set in both daytime and nighttime.

1. Introduction

Satellite infrared sounders were initially on board the Nimbus 6 satellite that was launched in 1975 and have been onboard National Oceanic and Atmospheric Administration (NOAA) Polar Orbiting Environmental Satellite (POES) series since then. The first High-Resolution Infrared Radiation Sounder (HIRS) onboard Nimbus 6 satellite had only 16 infrared channels and one visible channel. The follow-up HIRS instruments, HIRS2/3/4 on board the NOAA 6 to 19 had 19 infrared channels and one visible channel. These infrared channels are located within a spectral range of 650–2700 cm^{-1}. The HIRS channel with 1219.51 cm^{-1} central wave number was removed from and four new infrared channels were added to HIRS2/3/4. A new, more advanced infrared sounder called the Atmospheric Infrared Sounder (AIRS) has been on board on the National Aeronautics and Space Administration Aqua satellite since 4 May 2002. AIRS is a hyperspectral spectrometer and has 2378 channels. The second hyperspectral infrared sounder, the Infrared Atmospheric Sounding Interferometer (IASI), has been onboard Meteorological Operational satellite program A and B morning satellites, launched on 19 October 2006 and 17 September 2012, respectively. IASI provides 8461 spectral channels. The third hyperspectral infrared sounder is the Cross-track Infrared Sounder (CrIS), which has been on board the afternoon Suomi National Polar-Orbiting Partnership (SNPP) satellite launched on 28 October 2011.

Cloud detection is an important step that remains to be the largest source of uncertainty for satellite infrared data assimilation in numerical weather prediction (NWP). If cloud-affected radiances are treated as clear-sky measurements and then assimilated into NWP models, then the analysis fields would be biased and the NWP forecast skills could be significantly degraded. The optically thin cirrus clouds (e.g., optical depths less than 1) are more difficult to detect than thick clouds. Cirrus clouds regularly cover about 20% of the globe. They are optically thin due to a low concentration of ice particles, not lack of a significant amount of large, nonspherical ice crystals. *McNally and Watts* [2003] developed a cloud detection algorithm for high-spectral-resolution infrared sounders by comparing the difference spectrum between the observations and cloud-free model simulations (i.e., O-B^{clear}). In the presence of cloud, the O-B^{clear} difference spectrum would be closest to the B^{cloud}-B^{clear} difference spectrum, assuming that the simulated clear and cloudy spectra were free of error. However, errors in the simulations of the background clear and cloudy spectra and in the background atmospheric state itself can enter the minimum residual estimate.

An alternative algorithm for cloud detection is proposed in this study by taking an advantage of the large numbers of longwave infrared (LWIR) and shortwave infrared (SWIR) channels provided by CrIS. Based on an assumption that cloud emission and scattering intensities are different between LWIR and SWIR channels, SWIR and LWIR channels are paired and combined to derive a set of cloud emission and scattering indices (CESIs) that can capture cloud features in different layers of the atmosphere. The algorithm only involves simulations in clear-sky conditions, which is much more accurate than cloudy radiance simulations. The paper is organized as follows: Section 2 will briefly discuss the CrIS channel characteristics. Section 3 describes the CESI algorithm, which makes use of CrIS LWIR and SWIR paired channels. In section 4, the performance of the newly developed CESI for detecting optically thin clouds is demonstrated. Summary and conclusions are provided in section 5.

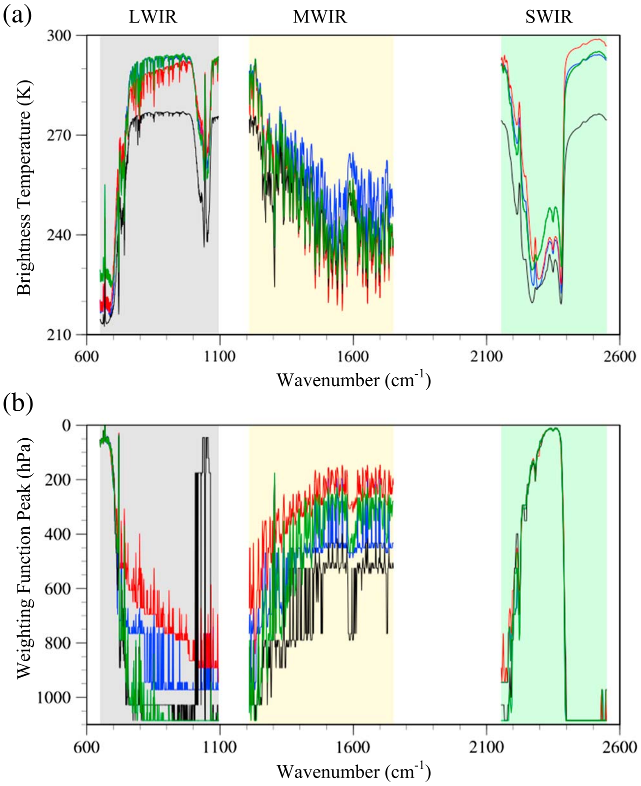

Figure 1. CRTM-simulated (a) brightness temperatures and (b) weighting function peaks for CrIS LWIR (gray shaded spectral region), MWIR (yellow shaded spectral region), and SWIR (green shaded spectral region) with four different input profiles: U.S. standard profile (green), the ECMWF profiles located at (29.8°N, 116°W) (blue), (28.7°N, 149.8°W) (red), and (47.3°S, 116.5°W) (black).

2. SNPP CrIS Channel Characteristics

CrIS onboard SNPP is a sophisticated cross-track scanning infrared sounding sensor that accurately measures upwelling infrared radiance at high spectral resolutions [*Glumb and Predina*, 2002]. It is a spaceborne Fourier transform spectrometer that is designed to achieve very low noise at high spectral resolution. CrIS represents a significant enhancement over NOAA's legacy infrared sounders (e.g., HIRS2/3/4) on board the Television Infrared Observation Satellite Operational Vertical Sounder series. The high spectral resolution with 1305 channels allows a high vertical sounding resolution be achieved by CrIS. The 1305 CrIS channels are located in the LWIR band of 650–1095 cm^{-1} at a spectral resolution of 0.625 cm^{-1}, the midwave IR (MWIR) band of 1210–1750 cm^{-1} at a spectral resolution of 1.25 cm^{-1}, and the SWIR band of 2155–2550 cm^{-1} at a spectral resolution of 2.5 cm^{-1} [*Han et al.*, 2013]. As the SNPP satellite moves, the hyperspectral infrared sounder CrIS observes a total of 30 field of regards (FORs) and nine fields of views (FOVs) within each FOR in the cross-track direction. The beam width for CrIS is 0.963°, corresponding to a 14 km diameter FOV at nadir. As expected for a cross-track scanning infrared sounding sensor, the sizes of both FOVs and FORs increase with scan angle. At the largest scan angle, the cross-track and along-track FOV diameters are about 39 km and 25 km, respectively.

Figure 1 provides brightness temperature (Figure 1a) and weighing functions (WFs; Figure 1b) simulations for LWIR, MWIR, and SWIR with the following four different input profiles: the U.S. standard profile and three European Centre for Medium-Range Weather Forecasts (ECMWF) profiles. The Community Radiative

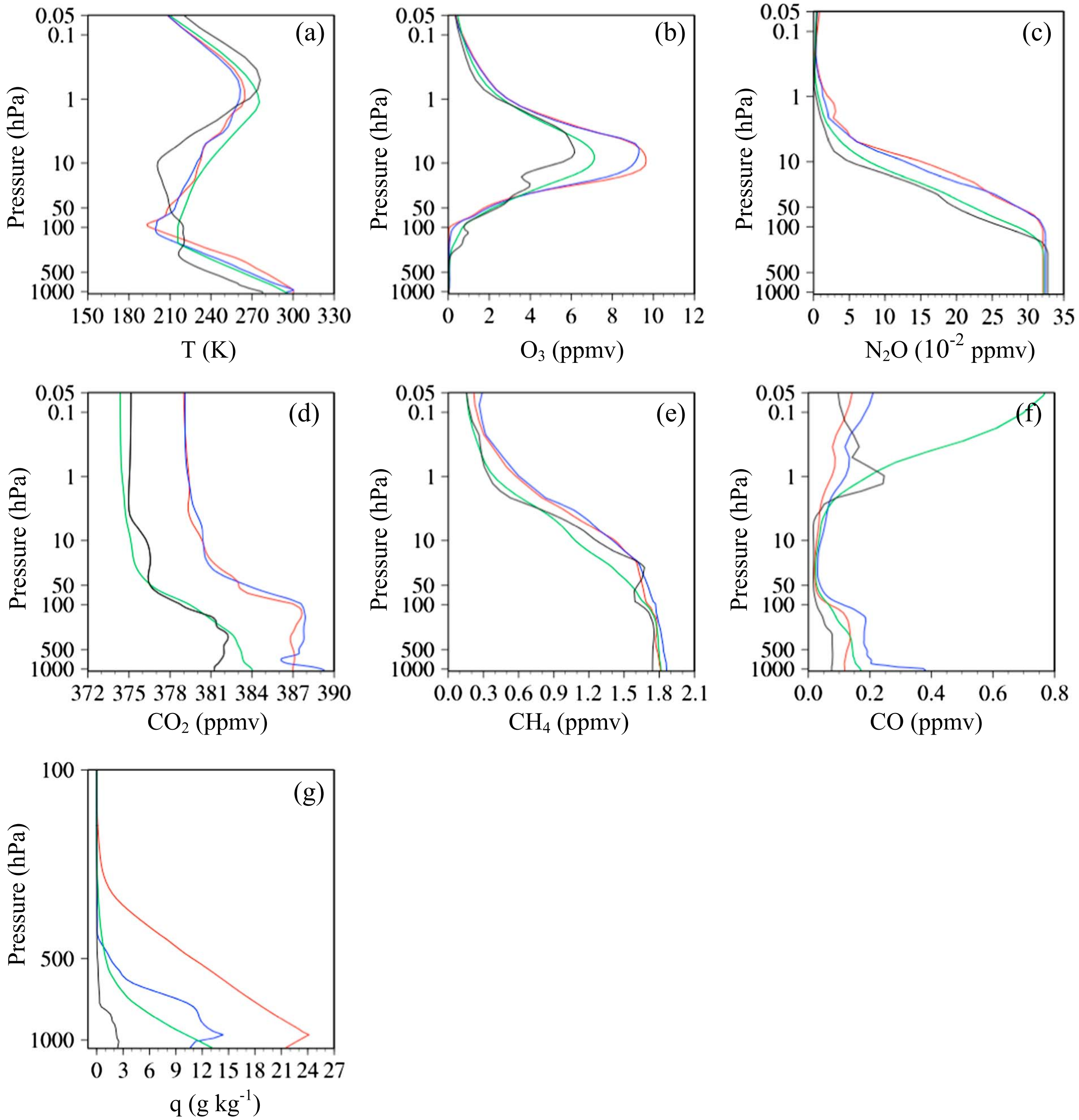

Figure 2. Vertical profiles of (a) temperature, (b) ozone, (c) nitrogen, (d) carbon dioxide, (e) methane, (f) carbon monoxide, (g) specific humidity, and (h) locations of ECMWF profiles (open circle) and the three input profiles (blue, red, and black dots) used in Figure 1.

Transfer Model (CRTM) that was developed by the U.S. Joint Center for Satellite Data Assimilation [*Weng*, 2007; *Han et al.*, 2007] is used for generating CrIS brightness temperatures and WFs shown in Figure 1. Both nonlocal thermodynamic equilibrium radiance correction scheme and a bidirectional reflectance distribution function to compute the solar reflection at 4.3 μm have been implemented into the current version of CRTM used for this study [*Chen et al.*, 2013]. The input profiles required by CRTM include the vertical profiles of temperature, ozone, nitrogen, carbon dioxide, methane and carbon monoxide, and specific humidity and are shown in Figures 2a–2g. The three input ECMWF profiles are extracted from the 83 ECMWF profiles that were chosen by *Chevallier et al.* [2006] for representing the range of variations in temperature and absorber amount found in the real atmosphere. The locations of these ECMWF profiles are shown in Figure 2h. The LWIR temperature channels located in the spectral region between 660 and

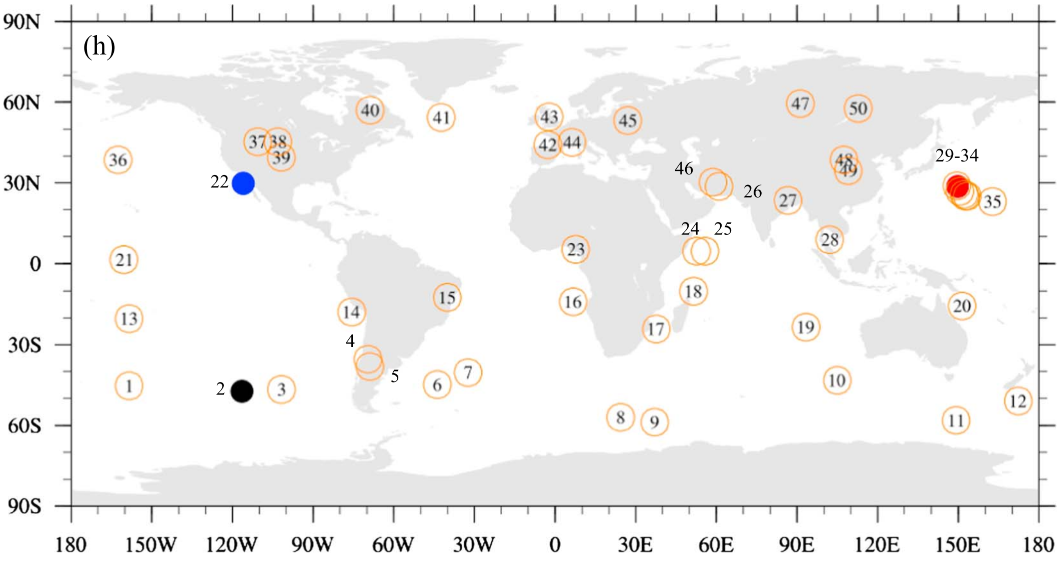

Figure 2. (continued)

750 cm^{-1} provide the vertical profiling of atmospheric temperature with high vertical resolution. The SWIR temperature channels (2200 to 2420 cm^{-1}) are for profiling the upper atmospheric temperature from 60 hPa to 10 hPa. Ozone channels are distributed over the spectral range of 990–1070 cm^{-1}. Water vapor channels distributed in the LWIR spectral range of 780–1210 cm^{-1} can provide the water vapor information near the surface and those distributed in the MWIR spectral range from 1310 to 1750 cm^{-1} enable the vertical profiling of the atmospheric water vapor from 800 to 200 hPa. Surface temperature channels are distributed over two spectral ranges 770–1095 cm^{-1} and 2460–2540 cm^{-1}. By comparing among four different simulations using four different inputs of atmospheric temperatures and absorber amounts, it is shown that a large variability of both the brightness temperatures and WF peak altitudes appear in several spectral regions.

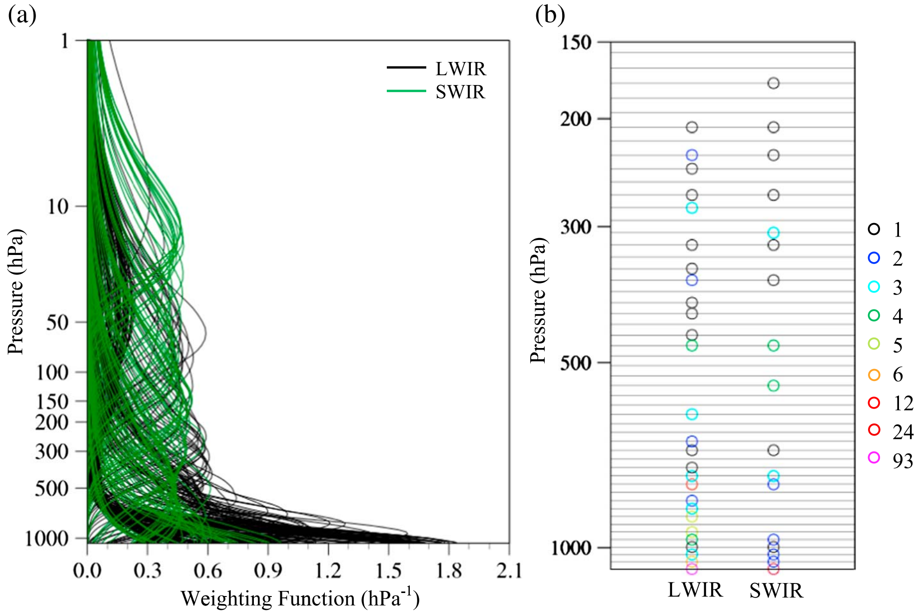

Figure 3. (a) WFs of 163 LWIR and 53 SWIR channels whose peak WFs are located below 150 hPa. (b) Total numbers of LWIR and SWIR channels that have the same peak WF altitude (colored circles).

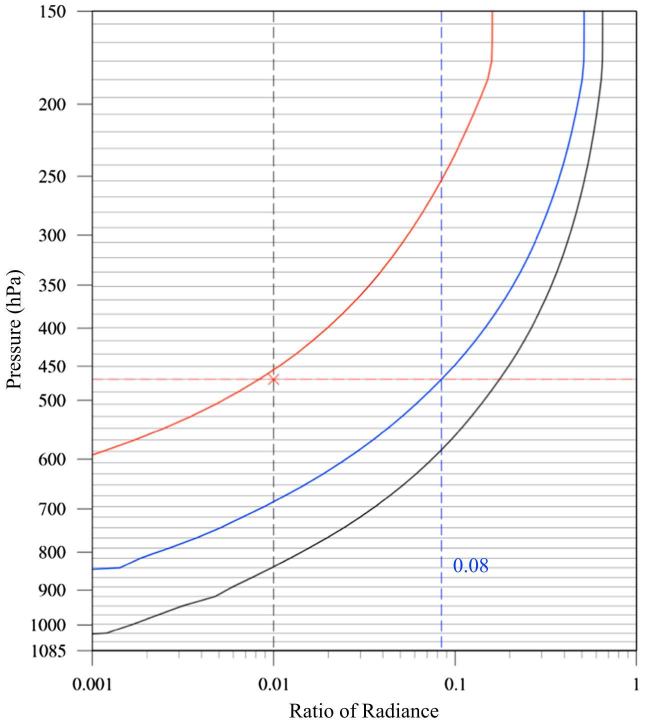

Figure 4. Ratio of $\frac{|R_{\text{clear}}-R_{\text{cloudy}}|}{R_{\text{clear}}}$ for LWIR channel 80 (699.375 cm^{-1}, red curve), and candidate paired SWIR channels 1187 (2255 cm^{-1}, black curve) and 1189 (2260 cm^{-1}, blue curve). The cloud-insensitive height of LWIR channel 80 is determined as the pressure level where the ratio becomes less than 0.01. The ratio at the same height for SWIR channel 1189 equals to 0.084.

3. A Cloud Detection Algorithm Using CrIS Double CO$_2$ Bands

Clouds modulate incoming shortwave solar radiation (visible and near infrared) by reflecting about 30% of the total amount of sunlight reaching the Earth. It is hypothesized that stronger ice particle scattering effects produce more significant depressions on the observed brightness temperatures of the SWIR CO$_2$ band than the LWIR CO$_2$ band in the presence of optically thin (e.g., cirrus) clouds. Likewise, the emission from optically thick clouds can also behave differently between longwave and shortwave channels. Thus, the hyperspectral infrared observations of the CrIS instrument are appropriate for detecting clouds including the optically thin clouds.

3.1. Pairing Between LWIR and SWIR Channels

In pairing the LWIR and SWIR channels, we only consider those CO$_2$ channels within LWIR 670–750 cm^{-1} and SWIR 2200–2400 cm^{-1} with their peak WFs located below 12 km. For each LWIR channel located within 670–750 cm^{-1} below 12 km, a SWIR channel satisfying the following conditions will be chosen to be paired with the LWIR channel:

1. The peak WF level of a candidate SWIR channel is the same or less than 50 hPa away from the peak WF level of the LWIR channel.
2. A cloud-insensitive level is determined as follows:

$$\left.\frac{\left|R^{\text{LWIR}}_{\text{clear}}-R^{\text{LWIR}}_{\text{cloudy}}\right|}{R^{\text{LWIR}}_{\text{clear}}}\right|_{P^{\text{LWIR}}_{\text{CS}}} \le 0.01\,, \quad \left.\frac{\left|R^{\text{SWIR}}_{\text{clear}}-R^{\text{SWIR}}_{\text{cloudy}}\right|}{R^{\text{SWIR}}_{\text{clear}}}\right|_{P^{\text{SWIR}}_{\text{CS}}} \le 0.1 \tag{1}$$

where $R^{\text{LWIR}}_{\text{cloudy}}\left(R^{\text{SWIR}}_{\text{cloudy}}\right)$ represents the CRTM-simulated cloudy radiance with an opaque cloud being located at the pressure level L_P, while all other input is the same as those for the clear-sky radiance $R^{\text{LWIR}}_{\text{clear}}$ $\left(R^{\text{SWIR}}_{\text{clear}}\right)$, where L_P varying from 150 hPa to the lower model level. The second condition can then be stated as follows: the cloud-insensitive level of the candidate SWIR channel satisfying the first condition is the same or less than 50 hPa away from the cloud-insensitive level of the LWIR channels. The cloud-insensitive level represents the lowest altitude below which the tail of the channel WF is small and radiation from the atmosphere below this level can be neglected. This second condition on cloud-insensitive level ensures the WFs of paired LWIR and SWIR channel to have similar vertical distributions.

3. The final SWIR channel to be paired with the LWIR channel shall not only satisfy the above two conditions but also has the smallest standard deviation of brightness temperatures from the LWIR channel brightness temperatures simulated for all input ECMWF profiles.

Both the peak weighting function altitudes required in step 1 and cloud-insensitive levels involved in step 2 of each channel are calculated by using the U.S. standard atmospheric profiles as input to CRTM. Figure 3a

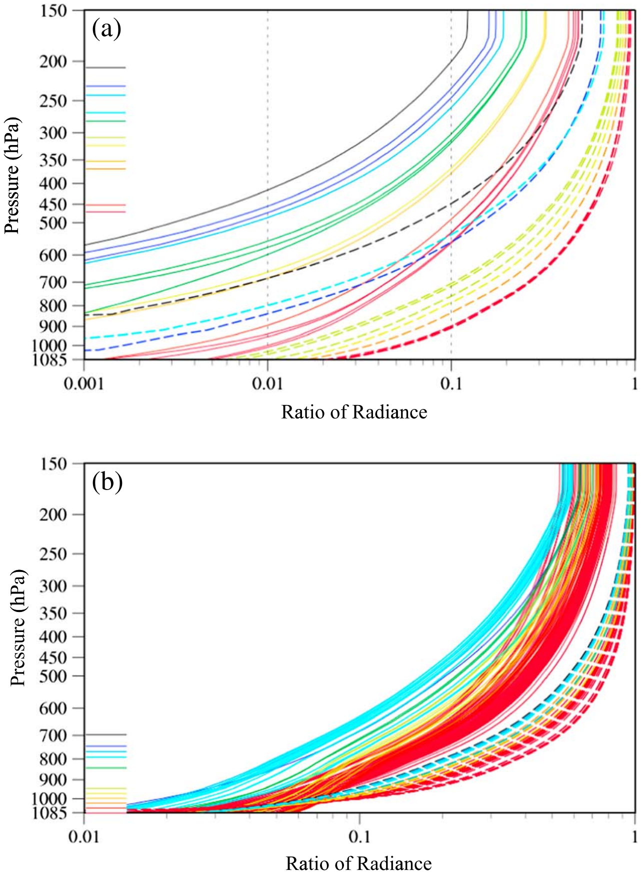

Figure 5. Ratio of $\frac{|R_{\text{clear}}-R_{\text{cloudy}}|}{R_{\text{clear}}}$ for (a) 14 LWIR and 12 SWIR channels whose peak WF altitude is above 500 hPa, and (b) 130 LWIR and 37 SWIR channels whose peak WF altitude is below 500 hPa. LWIR and SWIR channels are indicated by solid and dashed curves, respectively.

provides WF profiles of 163 LWIR and 53 SWIR channels that have their peak WFs located below 150 hPa and also are among those 184 LWIR, 128 MWIR, and 87 SWIR channels selected for NWP applications [*Gambacorta et al.*, 2012; *Gambacorta and Barnet*, 2013]. A larger number of channels with their WFs located at different altitudes allows a higher vertical resolution be achieved for the retrieval of the vertical profiles of atmospheric temperature and absorber amounts (e.g., water vapor, ozone, nitrogen, carbon dioxide, methane, and carbon monoxide). The shape of a WF profile determines the relative contribution of the atmospheric layer centered at the WF peak altitude; i.e., the atmosphere at the altitude of WF peak contributes most to the radiance observed by that channel. From Figure 3a, it is seen that both the LWIR and SWIR sounding channels are densely and evenly distributed in the troposphere and stratosphere. This allows a pairing between LWIR and SWIR channels for remote sensing of vertical structures of clouds. Among the channels selected for CrIS data assimilation in GSI, there are 163 LWIR and 53 SWIR channels that have peak weighting functions below 150 hPa and are located at 27 and 17 different pressure levels, respectively. The pressure levels and the total numbers of LWIR and SWIR channels that have the same peak WF altitude are provided in Figure 3b. This allows the first step of the pairing between LWIR and SWIR channels described above to be completed.

The second step of the LWIR/SWIR pairing is illustrated in Figures 4 and 5. Figure 4 shows the variations of the ratio $\frac{|R_{\text{clear}}-R_{\text{cloudy}}|}{R_{\text{clear}}}$ for one LWIR channel 80 (699.375 cm^{-1}, red curve), and two candidate SWIR channels 1187 (2255 cm^{-1}, black curve) and 1189 (2260 cm^{-1}, blue curve) with respect to pressure. The peak WF levels of these two SWIR channels are the same or less than 50 hPa away from the peak WF level of LWIR channel 80. The cloud-insensitive height of LWIR channel 80 is defined as the model level at which the ratio becomes less than 0.01 (see the red dashed horizontal line in Figure 4). The ratio of the SWIR channel 1189 at the

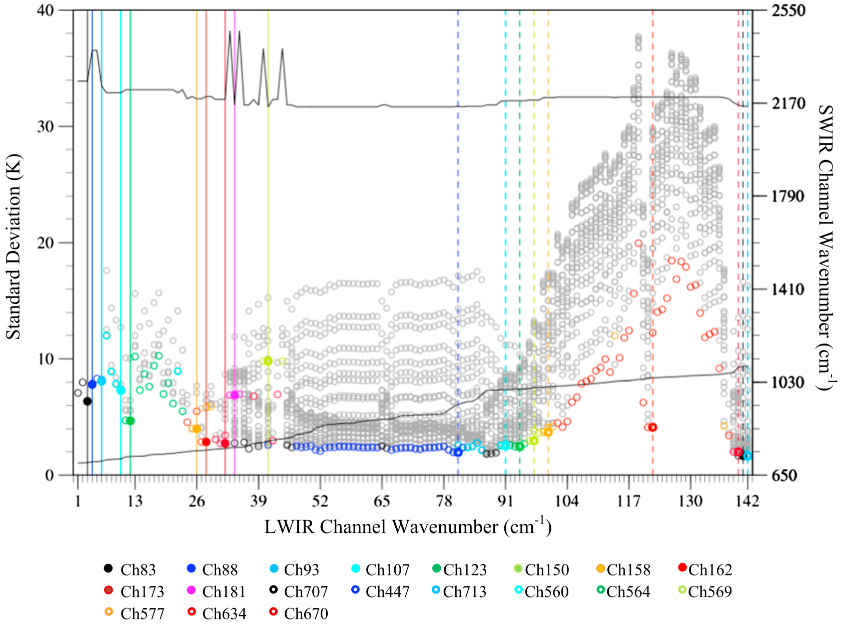

Figure 6. Root-mean-square deviation (RMSD) between the paired LWIR and SWIR channels that passed steps 1 and 2 (grey circles). The *x* axis represents 142 LWIR channels left after steps 1 and 2; they are ordered from lower to higher wave number. The minimum RMSD is indicated by colored symbols, with the final selected pairs being indicated by solid symbols. There are 19 pairs identified, and the 19 SWIR channels are color-coded.

cloud-insensitive pressure level of the LWIR channel is equal to 0.084, which is smaller than the threshold of 0.1 defining the cloud insensitivity for SWIR channels. The ratio of the SWIR channel 1187 at the cloud-insensitive pressure level of the LWIR channel is greater than the threshold of 0.1 of the ratio of the SWIR channels. Therefore, SWIR channel 1189 is selected for pairing with LWIR channel 80. Figure 5 presents the variations of the ratio $\frac{|R_{\mathrm{clear}}-R_{\mathrm{cloudy}}|}{R_{\mathrm{clear}}}$ for 14 LWIR and 12 SWIR channels whose peak WF altitude is above 500 hPa

Table 1. Channel Number, Wave Number, Peak WF Pressure, and Cloud-Insensitive Level Pressure for 19 Paired LWIR and SWIR Channels

	LWIR				SWIR			
Pair	Channel Number	Wave Number (cm^{-1})	Peak WF Height (hPa)	Cloud-Insensitive Height (hPa)	Channel Number	Wave Number (cm^{-1})	Peak WF Height (hPa)	Cloud-Insensitive Height (hPa)
1	23(83)	701.250	229	487	348(1189)	2260.000	206	451
2	26(88)	704.375	280	586	383(1239)	2385.000	266	545
3	28(93)	707.500	321	672	346(1181)	2240.000	307	718
4	36(107)	716.250	469	1028	336(1170)	2212.500	469	1085
5	41(123)	726.250	790	1085	341(1175)	2225.000	766	
6	57(150)	743.125	840		340(1174)	2222.500	790	
7	63(158)	748.125			330(1164)	2197.500		
8	67(162)	750.625	972		326(1160)	2187.500	972	
9	75(173)	757.500			325(1159)	2185.000	1000	
10	77(181)	762.500	1028		392(1271)	2465.000	1085	1028
11	182(707)	1091.250	1057		316(1150)	2162.500		1085
12	122(447)	928.750	1085		313(1147)	2155.000		
13	184(713)	1095.000			314(1148)	2157.500		
14	132(560)	999.375			322(1156)	2177.500		
15	135(564)	1001.875			323(1157)	2180.000		
16	138(569)	1005.000			324(1158)	2182.500		
17	141(577)	1010.000			328(1162)	2192.500	1057	
18	163(634)	1045.625			329(1163)	2195.000	1028	
19	181(670)	1068.125			320(1154)	2172.500	1085	

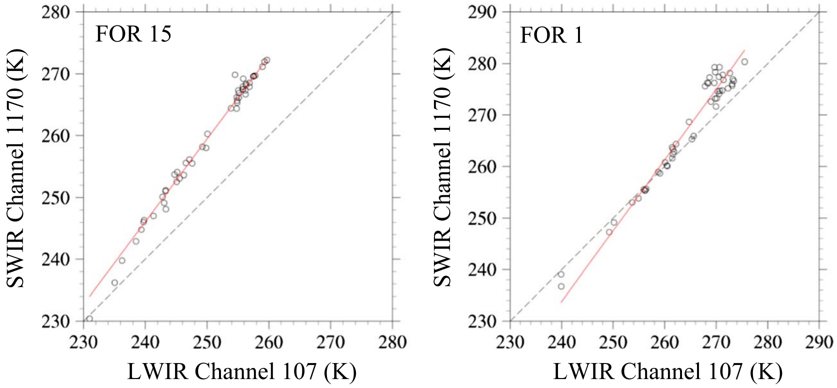

Figure 7. Scatterplots of brightness temperatures of LWIR channel 107 (716.25 cm^{-1}) that is paired with SWIR channel 1170 (2212.5 cm^{-1}) simulated in clear-sky conditions at FORs 1 and 15.

(Figure 5a) as well as 130 LWIR and 37 SWIR channels whose peak WF altitude is below 500 hPa (Figure 5b). It is seen that SWIR channels are generally more sensitive to the presence of clouds than LWIR channels.

After completing the first two steps for the pairing between two CO$_2$ bands: LWIR 670–750 cm^{-1} and SWIR 2200–2400 cm^{-1}, it is possible that a single LWIR channel could be paired with more than one SWIR channel and vice versa. The third step is executed to determine the final LWIR/SWIR matching pair. For this purpose, the standard deviations of brightness temperatures between a LWIR channel and all its paired SWIR channels after steps 1 and 2 simulated with the ECMWF profiles (see Figure 2h) as input are calculated and shown in Figure 6. The SWIR channel that has the smallest standard deviation is selected in step 3. A total of 19 pairs remain after finishing the three-step pairing procedure. Table 1 lists the channel number, wave number, peak WF pressure, and cloud-insensitive level pressure for these 19 LWIR/SWIR paired channels. A total of three, one, and five pairs are found in the upper, middle, and low troposphere, respectively. The remaining pairs are at surface or near surface.

3.2. The Cloud Emission and Scattering Index (CESI)

Once the pairing between LWIR and SWIR CO$_2$ channels is completed, a linear regression model is established for each channel:

$$T^{\mathrm{SWIR}}_{b,i,\mathrm{regression}} = \alpha_i T^{\mathrm{LWIR}}_{b,i,\mathrm{CRMclear}} + \beta_i \tag{2}$$

where the subscript "*i*" represents the number of pairs and α_i and β_i are the regression coefficients whose values are obtained by minimizing the following cost function:

$$\min J(\alpha_i, \beta_i) = \sum_{j=1}^{50} \left(T^{\mathrm{SWIR}}_{b,i,\mathrm{regression}}(j) - T^{\mathrm{SWIR}}_{b,i,\mathrm{CRTMclear}}(j) \right)^2 \tag{3}$$

where the subscript "*j*" represents the 50 ECMWF profiles under clear-sky assumptions. Also, the fifth (center) FOV in each CrIS FOR is used for regression.

Figure 7 provides scatterplots of CRTM simulated brightness temperatures at two different FORs (e.g., FORs 1 and 15) for a paired channels with the peak WFs located around 469 hPa: LWIR channel 107 (716.25 cm^{-1}) and SWIR channel 1170 (2212.5 cm^{-1}). The brightness temperature simulations are obtained by using a diverse set of ECMWF analysis profiles, which were chosen by *Chevallier et al.* [2006] for representing the range of variations in temperature and absorber amount found in the real atmosphere. It is pointed out that the sun glint effect of solar radiation on SWIR radiances, which is more significant when the sun glint smaller, cannot be simulated without knowing the local times of these profiles. A linear relationship between the two-paired channels is found at both FORs. The slopes of the variation of LWIR brightness temperatures with respect to SWIR brightness temperatures are greater than 1. The LWIR brightness temperatures are lower

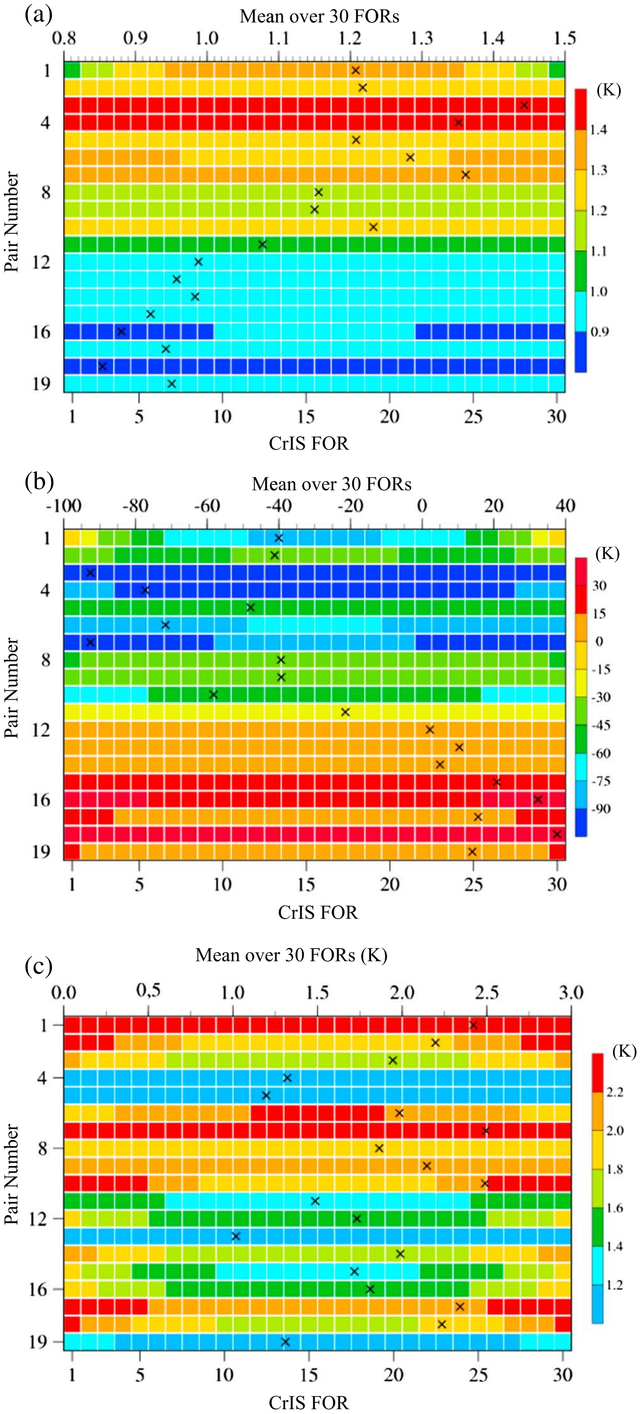

Figure 8. (a) Regression coefficients α, (b) coefficients β, and (c) standard deviations of the regression model error ($T_{b,\text{regression}}^{\text{SWIR}} - T_{b,\text{CRTMclear}}^{\text{SWIR}}$) for 30 FORs of the 19 pairs. The mean values averaged over all FORs are indicated by black crosses (top x axis).

than the SWIR brightness temperatures at FOR 15 and are higher than those at FOR 1. The linear regression model in equation (2) is the straight red line in Figure 7.

The regression coefficients α and β in equation (2) for the 30 FORs of the 19 pairs are shown in Figures 8a and 8b. It is seen that the slope (α) and the intercept (β) of the regression equations between LWIR and SWIR channels have not only a strong channel dependence but also a weak scan angle dependence. The values

Table 2. CESIs Calculated From Simulated Brightness Temperatures for Optically Thin and Thick Clouds

		CESI (K)	
Pair	Peak WF Height (hPa)	Optically Thin Cloud	Optically Thick Cloud
1	229	5.24	−3.14
2	280	5.44	−4.15
3	321	3.53	−2.16
4	469	4.33	−0.66
5	790	4.21	−0.43
6	840	5.72	−6.33

of α and β, at individual FORs deviate from their mean values, which are shown by black crosses in Figure 8. This suggests a necessity of carrying out the linear regression FOR-by-FOR, a result from a cross-track scanning sensor. An error estimate for the regression model is provided in Figure 8c. It is seen that the standard deviations of the regression model error ($T^{SWIR}_{b,regression} - T^{SWIR}_{b,CRTMclear}$) for 30 FORs of the 19 pairs are less than 2.4 K.

A cloud emission and scattering index (CESI) can finally be defined as follows:

$$\mathrm{CESI}_i = T^{\mathrm{SWIR}}_{b,i,\mathrm{regression}}\left(T^{\mathrm{LWIR}}_{b,i,\mathrm{obs}}, \alpha_i, \beta_i\right) - T^{\mathrm{SWIR}}_{b,i,\mathrm{obs}} \tag{4}$$

where

$$T^{\mathrm{SWIR}}_{b,i,\mathrm{regression}} = \alpha_i T^{\mathrm{LWIR}}_{b,i,\mathrm{obs}} + \beta_i \tag{5}$$

CESI reflects a differential scattering between LWIR and SWIR CO_2 spectral bands. CO_2 in the atmosphere has a radiative transition of energy in its vibration mode, resulting in two absorption/emission bands: one is referred as the ν2 band near 15 μm (667 cm^{-1}) and the other as ν3 band near 4.3 μm (2349 cm^{-1}). The absorption coefficient at a wavelength or channel is typically a function of absorption line strength and line shape. From Lorenz profile, the half width of line shape is a function of pressure (P) and temperature (T). Thus, for a channel within ν2 or ν3 band, the energy emitted from the atmosphere is sensitive to the temperature at a particular atmospheric pressure level. By carefully matching the weighting function peak heights from two channels at CrIS ν2 band (LWIR) or ν3 band (SWIR), their brightness temperatures under clear-sky conditions can be strongly correlated. In this study, a linear regression is used to quantify such relationship. When an optically thin cloud occurs in the atmosphere, LWIR channel is assumed to be unaffected by the cloud scattering, and thus, its brightness temperature can be used to estimate the SWIR brightness temperature at the cloud base from the linear regression relationship. Therefore, the difference between SWIR brightness temperatures observed from the cloud top and estimated from LWIR channel can be used to detect the scattering from the thin cirrus clouds.

For further understanding of the effect of optically thin and thick clouds on CESI, the LWIR and SWIR brightness temperatures are simulated and compared by using CRTM for optically thin and thick clouds, respectively. A cloud with a thickness of 1.5 km and an effective radius of ice particle of 30 μm is placed at the peak weighting function height of each paired LWIR and SWIR channels. The ice water path for the optically thin and thick cloud is set to be 5 and 400 g m^{-2}, respectively. Moreover, the U.S. standard atmospheric profiles are used for this simulation test. Table 2 compares the magnitudes of six-paired CESIs for the two cloud types. It is found that for an optically thin, CESI is positive and for an optically thick cloud, CESIs are negative.

4. Winter Storm Blizzard 2016 Observed by Satellites

A monster winter storm started in the afternoon of 22 January 2016 and ended in the early morning of 24 January 2016 over the eastern part of the United States, extending from Kentucky valley to New York City. This winter storm is named as the Blizzard 2016. It affected more than 85 million people due to its large amount of snow accumulation, strong wind, lightening, and freezing precipitation. Snowfall totaled more

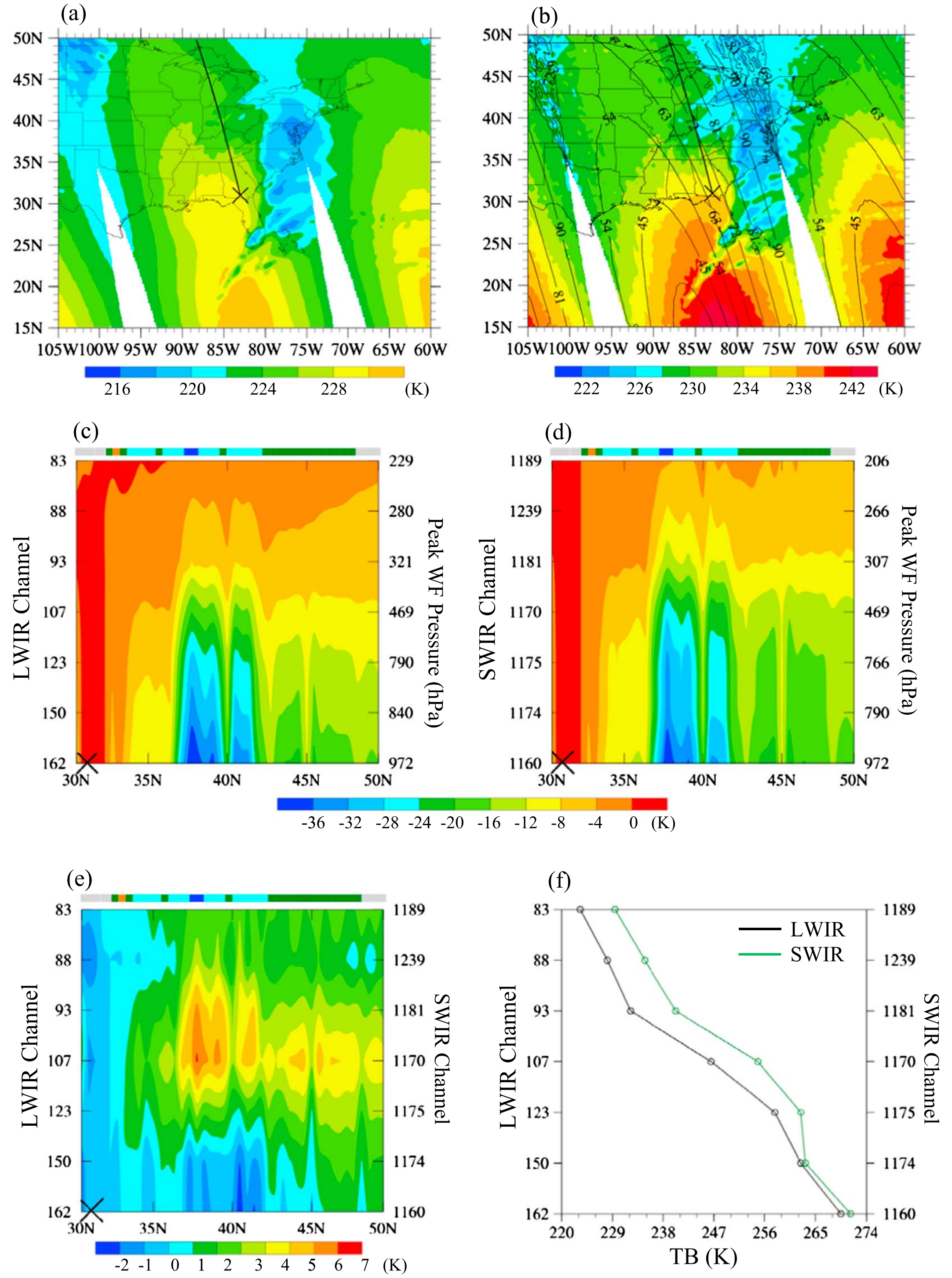

Figure 9. Spatial distributions of brightness temperatures for a paired channels with peak WF around 273 hPa: (a) LWIR channel 88 (704.375 cm^{-1}) and (b) SWIR channel 1239 (2385 cm^{-1}) along with sun glint angle (black contour) at the CrIS ascending node of SNPP on 22 January 2016. The local observing time is around 13:55 EST. Cross sections of brightness temperatures of seven (c) LWIR and (d) SWIR channels in the along-track direction through Blizzard 2016 along the black line in Figure 9a or Figure 9b starting from the center of Blizzard 2016 that is located at (83°W, 31°N) and indicated by a cross symbol. (e) Cross section of the difference between LWIR and SWIR (i.e., Figure 9c minus Figure 9d). (f) Brightness temperatures of seven LWIR (black curve) and SWIR (green curve) channels at the center of Blizzard 2016. The GOES 13 cloud types along the cross section are indicated by a color bar on top of Figures 9c–9e with supercooled water cloud in green, cirrus in cyan, opaque ice cloud in blue, and clear-sky in grey.

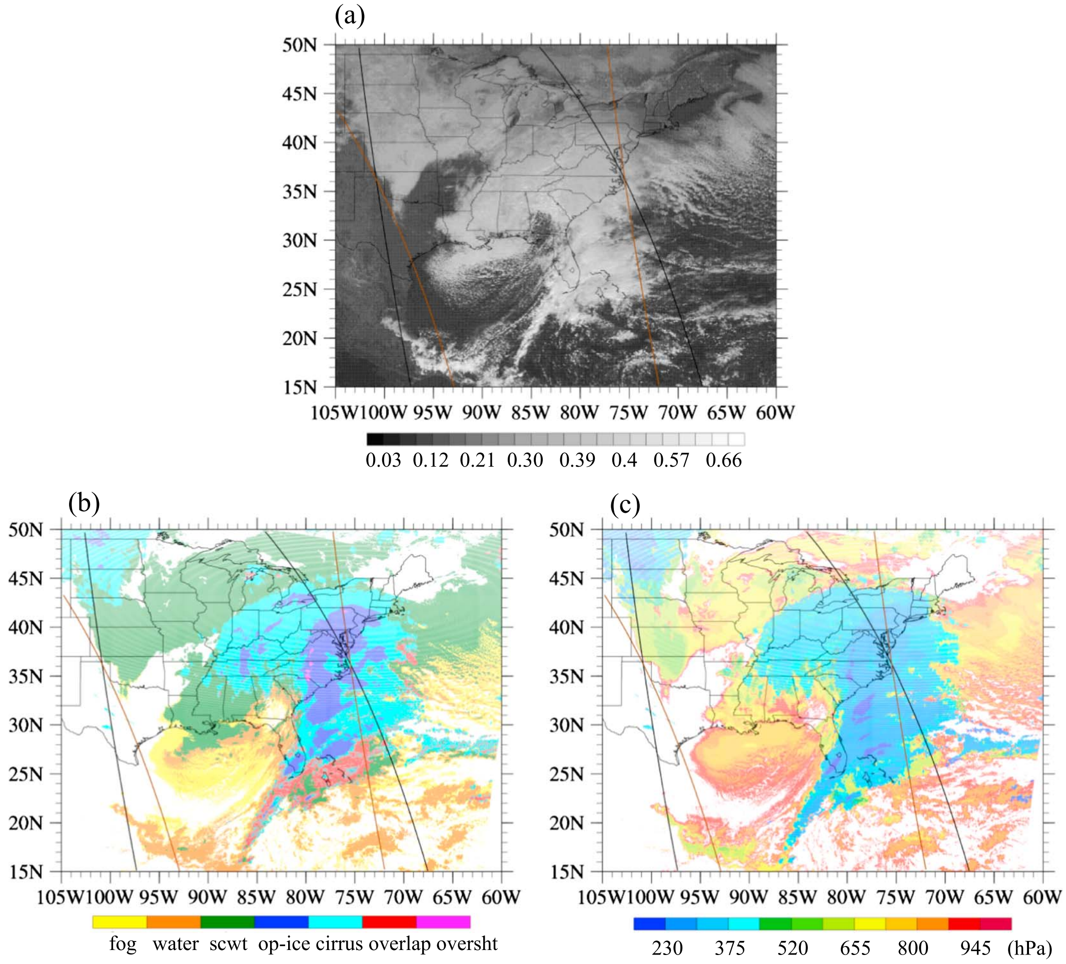

Figure 10. (a) GOES 13 reflectance of visible channel; (b) seven different cloud types of fog (yellow), water (orange), supercooled water (scwtr, green), opaque ice (op-ice, blue), cirrus (cyan), overlapping (overlap, red), and overshooting (oversht, purple) clouds; and (c) cloud top pressures at 1855 UTC (i.e., 13:55 EST) on 22 January 2016.

than 26 inch in Central Park of New York, 33.5 inch in Germantown of Maryland, and 40 inch over Shepherdstown in West Virginia. During the storm period, SNPP CrIS data were collected and the CESI algorithm developed in the previous section is applied to study the cloud properties associated with this historical winter storm.

The CrIS onboard SNPP provides twice-daily observations of Blizzard 2016 around local times 13:55 EST (day time) and 01:45 EST (nighttime) near Washington DC at SNPP's ascending and descending nodes, respectively. The horizontal and spectral distributions of brightness temperature observations of a selected LWIR/SWIR pair at the ascending node of SNPP on 22 January 2016 are provided in Figures 9a and 9b. It is noticed that the sun glint angles are greater than 36° in regions of interest except near the south edge of the domain, implying a negligible effect of contamination of short-wave radiances by solar radiation for the results presented in this region of interest. The center of Blizzard 2016 was located at (83°W, 31°N) at this time, which is indicated by a cross symbol in Figures 9a and 9b. Since CrIS is a cross-track scanning infrared sounding sensor, the brightness temperatures have an obvious scan-dependent feature. A comma-type cloud-like cold brightness temperature distribution is located in the northeast and east sides of the storm center. However, the depression in brightness temperature seems to be more widespread in the SWIR channel (Figure 9b) than in the LWIR channel (Figure 9a). The brightness temperature varies from a minimum 214 K to a maximum of around 230 K for LWIR channel 88 (704.375 cm^{-1}), with its low brightness temperatures located to the northeast of Blizzard center (Figure 9a). For SWIR channel 1239 (2385 cm^{-1}), the brightness temperature varies from a minimum 220 K to a maximum of around 244 K (Figure 9b). It is pointed out

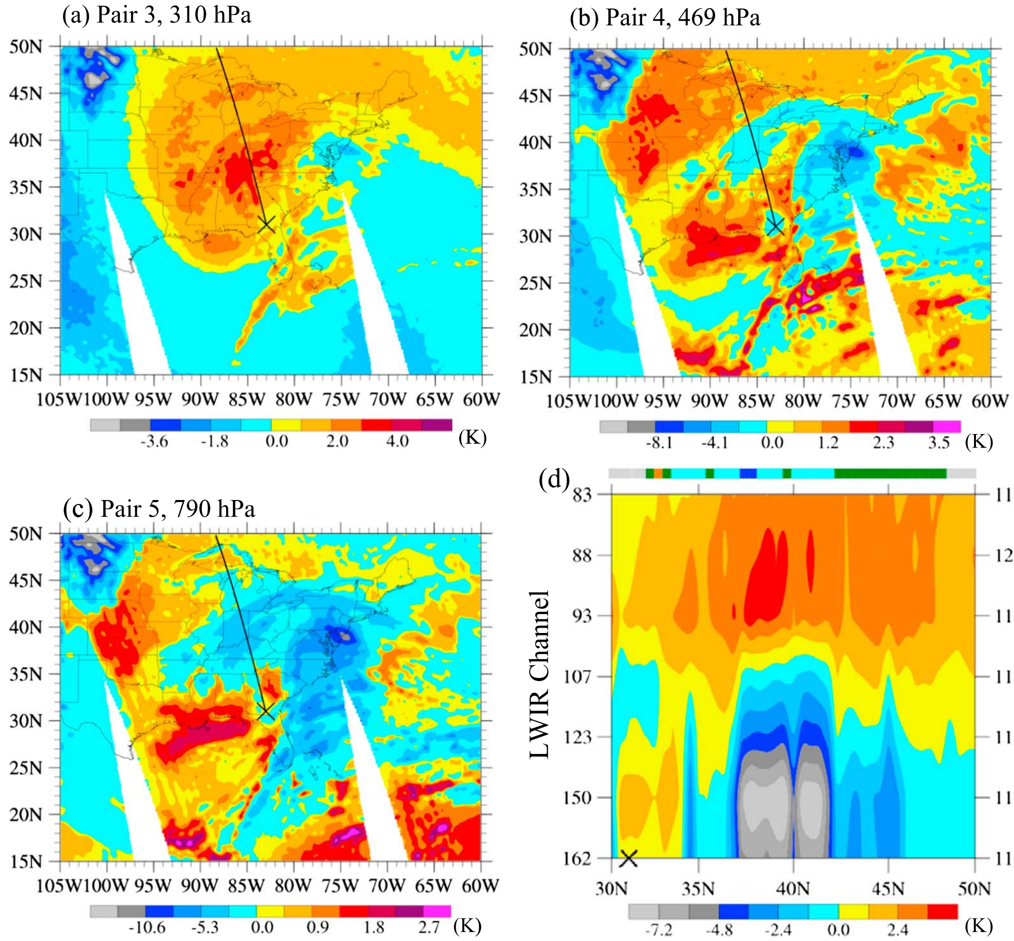

Figure 11. (a–c) Spatial distributions of CESI derived from the three LWIR/SWIR pairs and (d) cross section of CESI for first six and the eighth pairs in the along-track direction (e.g., the black line in Figures 11a–11c) from the center of Blizzard 2016 that is located at (83°W, 31°N) to 50°N on the ascending node of SNPP on 22 January 2016. The local observing time is around 13:55 EST. The GOES 13 cloud types along the cross section are indicated by a color bar on top of Figure 11d with supercooled water cloud in green, cirrus in cyan, opaque ice cloud in blue, and clear-sky in grey.

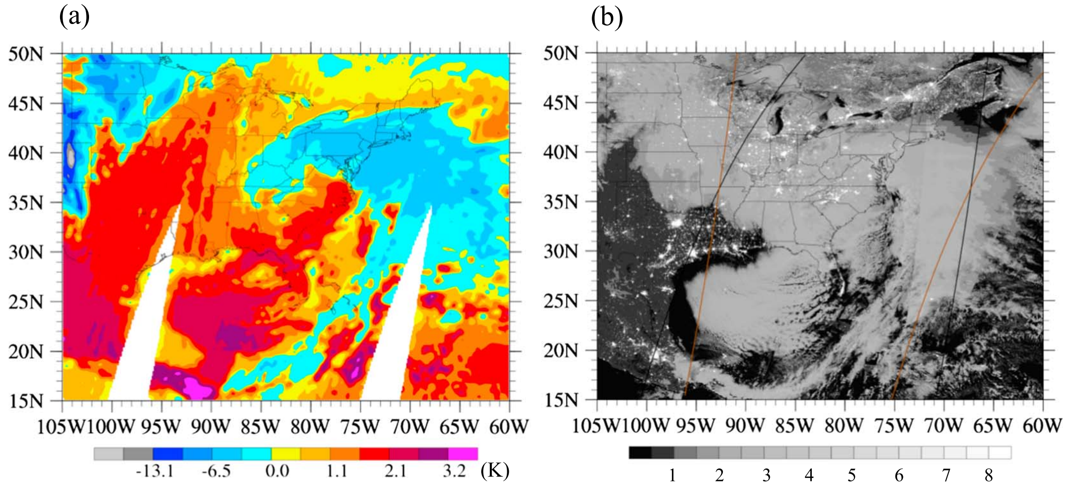

Figure 12. Spatial distributions of (a) CESI derived from the pair 5 (~778 hPa) at the descending node of SNPP and (b) VIIRS DNB radiance (unit: 10^{-8} W cm^{-2} sr^{-1}) around 0712 UTC (nighttime ~02:12 EST) on 23 January 2016.

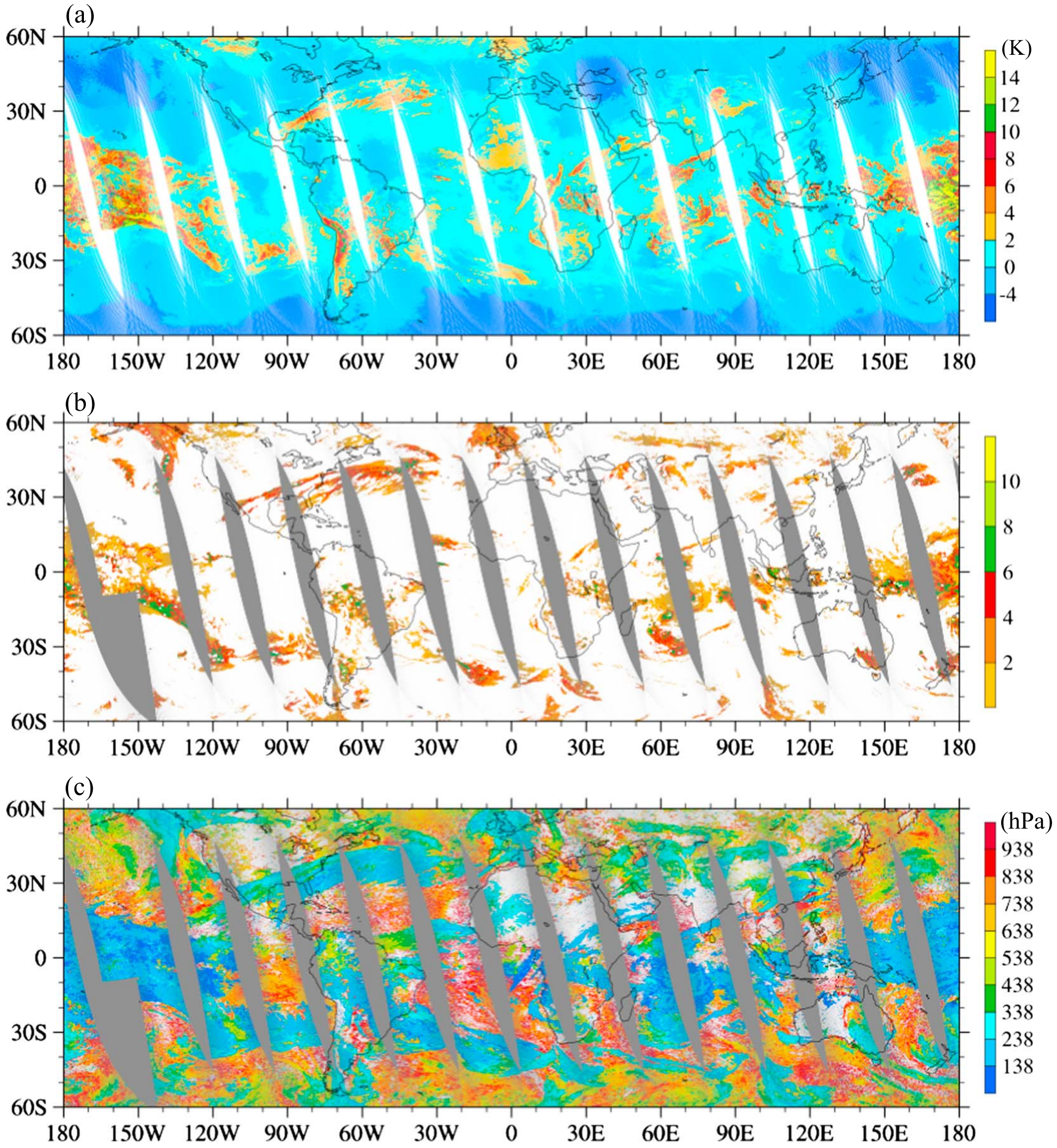

Figure 13. Spatial distributions of (a) CESI of pair 3 (~321 hPa), (b) AIRS version 6 ice cloud optical depth, and (c) AIRS version 6 cloud top pressure at CrIS ascending node on 1 January 2016.

that the brightness temperatures at eastern side of the CrIS swath are warmer than those at the western side near the storm center, indicating a weak warm anomaly in the storm center.

Figures 9c and 9d show an along-track cross section of CrIS LWIR and SWIR channel brightness temperatures that pass through the center of the storm. The limb effect of cross-track radiometer on brightness temperature is avoided in such cross sections along a fixed scan angle. The brightness temperatures at the center of the Blizzard 2016 (Figure 9f) are subtracted from Figures 9c and 9d. The brightness temperatures in the cloudy regions are more than several tens degrees colder than its surrounding clear streaks. The SWIR brightness temperatures are, in general, higher than those of LWIR channels in cloudy conditions. The brightness temperatures of all channels near the center of the Blizzard 2016 are the warmest along the cross section. The SWIR brightness temperatures are more than several degrees warmer and a few degrees colder than the LWIR channels in the cloudy and clear-sky conditions, respectively (Figure 9e). Such a large contrast of brightness temperatures between LWIR and SWIR channels confirms the possibility of using CrIS double CO_2 bands to capture the thermal and cloud structural features of winter blizzard storms.

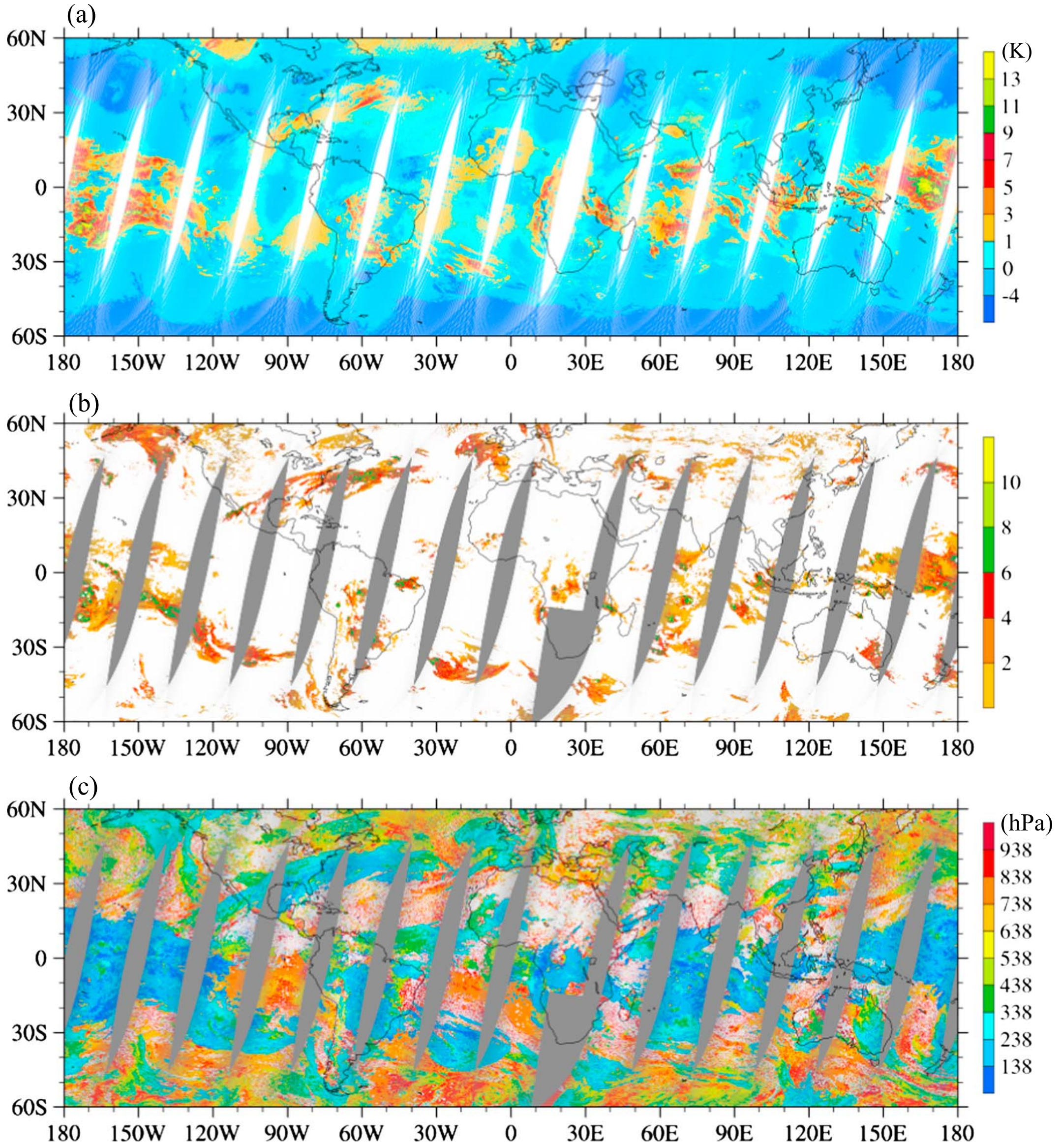

Figure 14. Same as Figure 13 except for CrIS descending node on 1 January 2016.

In order to further understand the cloud characteristics of Blizzard 2016, we can examine a spatial distribution of the Geostationary Operational Environmental Satellite (GOES) 13 imager visible channel reflectance (Figure 10a), as well as the cloud types and cloud top pressures (Figures 10b and 10c) that were derived from visible and infrared data [*Schreiner and Schmit*, 2002; *Heidinger and Straka III*, 2013] at 1855 UTC on 22 January 2016. A total of seven different cloud types are found to exist within and arround the storm (Figure 10b). The opaque ice, cirrus, overlapping, and overshooting clouds have high cloud tops whereas fog, water cloud, and supercooled water clouds are associated with cloud top pressures greater than 750 hPa (Figure 10c). The areas with heavy snow from Blizzard 2016 are indicated as blue color.

These GOES 13 cloud products can be used as a reference for examining the spatial distributions of CESIs derived from CrIS CO_2 pairs 3 to 5 shown in Figures 11a–11c. It is seen that the cloud structures and their vertical variations revealed in Figure 9 are well captured by the CESI. In particular, the pair 3 CESI is characterized by positive CESI values ranging between 2 and 4 K in cirrus clouds (cyan in Figure 10b) with their cloud top pressure between 300 and 375 hPa; the pair 4 CESI has positive CESI values around 1–2 K in the supercooled water clouds (scwt, green in Figure 10b) whose cloud top pressure are between 450 and 700 hPa. The lower level water clouds and fog with their cloud top pressures between 655 and 800 hPa are captured by the CESI of pair 5 with its values ranging from 2 to 3 K. Figure 11d shows a cross section of CESI for the first six and the eighth CrIS CO_2 pairs from the center of Blizzard 2016, which is located at (83°W, 31°N), to 50°N in the along-track direction (see the black line in Figures 11a–11c) on the ascending node of SNPP on 22 January 2016. The local observing time is around 13:55 EST. Areas with positive and negative CESI indicate the vertical distribution of optically thin and thick clouds, respectively.

Figure 12 presents a spatial distribution of CESI of pair 5 defined by the LWIR channel 123 (726.25 cm^{-1}) and SWIR channel 1175 (2225.0 cm^{-1}) (Figure 12a) on the descending node of SNPP around 0712 UTC (nighttime ~02:12 EST) on 23 January 2016. This pair is located around 778 hPa. Because the GOES 13 imager cloud products are not reliable during the nighttime, the day/night band (DNB) reflectance from the Visible Infrared Imaging Radiometer Suite (VIIRS), which is also on board SNPP, can be used for a qualitative validation of CESI (Figure 12b). VIIRS DNB band is designed with a high sensitivity to observe the clouds from reflected lunar radiation [*Walther and Heidinger*, 2013; *Cao et al.*, 2013]. In the evening of 22 January, the sky is clear with a full moon and is an ideal condition for VIIRS DNB data to be used for monitoring clouds. Indeed, the VIIRS DNB data have been widely used for monitoring the storms at high latitudinal areas such as Alaska during the winter season when GOES and POES solar visible data are unavailable. It is seen that the CESI is positive in clouds and negative in clear sky. The VIIRS DNB (Figure 12b) compares favorably with the CESI distribution around 778 hPa (Figure 12a). The low-level water clouds and fogs in Gulf of Mexico are also well captured by the positive CESI distributions with the magnitude range of 2–3 (Figure 12a). After the storm moving away from the east coast, the city lights are visible from VIIRS DNB bands and are shown as brightest pixels over the snow-covered land in the eastern part of U.S.

AIRS science team has made great accomplishments for retrieving cloud products from the AIRS and advanced microwave sounding unit (AMSU) instrument suite through more than a decade of research [*Kahn et al.*, 2014]. We can also apply this cloud detection algorithm globally and compare the CESI distributions with AIRS cloud products. Figures 13 and 14 provide such comparisons for the ascending (Figure 13) and descending (Figure 14) nodes on 1 January 2016. Specifically, spatial distribution of CESI for pair 3 CESI (~321 hPa; Figure 13a) are compared with AIRS ice cloud optical depth obtained from the AIRS version 6 data set (Figure 13b). The AIRS cloud top pressure on the same day (Figure 13c) is also provided for convenience. Most ice clouds are located above 338 hPa during both daytime and nighttime (Figures 13b and 13c and 14b and 14c). The global distribution of CESIs based on CrIS double CO_2 bands with peak weighting function at 321 hPa agrees well with the spatial distribution of ice cloud optical thickness at both the ascending and descending nodes.

5. Summary and Conclusions

The SNPP CrIS has provided us a unique data source for monitoring atmospheric temperature, water vapor, and cloud over the globe. A combined use of the dual CO_2 absorption band sounding channels located in the LWIR and SWIR bands allows us to develop a new method for detecting optically thin clouds. In this study, a cloud emission and scattering index (CESI) is developed from the LWIR and SWIR paired-channel measurements and its numerical procedures are carefully described. Using the Blizzard 2016 as an example, we demonstrated that the vertical and horizontal structures of optically thin clouds within and around the winter storm are successfully detected. The global distributions of CESI at 321 hPa compared well with the distributions of AIRS ice cloud optical depth contained in the AIRS version 6 cloud product data set.

The proposed CESI algorithm can be directly extended to the CrIS full spectrum resolution data for more detailed cloud vertical structures. This algorithm is useful for a direct detection and monitoring of clouds located at different altitudes and will benefit the NWP data assimilation by providing an improved quality control of cloud-affected radiances, especially those optically thin clouds such as cirrus and low stratus and fogs. However, for these applications, the effects of solar radiation on CrIS shortwave through nonlocal thermodynamic equilibrium effects during daytime and the solar radiation as a source term in radiative transfer equation, which are already taken care of in CRTM [*Chen et al.*, 2013], must be included for generating the regression coefficients by using a training data set with information on local times.

In the current NWP data assimilation systems, cloud detection for a satellite instrument (such as CrIS) has to be conducted based on the assimilated brightness temperature observations in the sensor data record of the same instrument (e.g., CrIS). Assimilation of the retrieved environmental data record (EDR) temperature and specific humidity profiles from the AIRS/AMSU [*Aumann et al*., 2003; *Chahine et al*., 2006; *Kahn et al*., 2014] or similarly CrIS/Advanced Technology Microwave Sounder (ATMS) could be a future alternative. The high-quality key cloud parameters that can be retrieved along with the retrieved temperature and specific humidity profiles from CrIS/ATMS can then be used for an effective cloud detection of CrIS/ATMS EDR data assimilation. Estimation and incorporation of observation error covariance matrix, which could be nondiagonal, into any NWP data assimilation systems are the most challenging problem for satellite EDR data assimilation.

Acknowledgments
The views expressed in this publication are those of the authors and do not necessarily represent those of NOAA. This research work was jointly supported by the JPSS Proving Ground and Risk Reduction (PGRR) Program (project NA14NES4320003) and HFIP project (project NA15NWS4680002). The data used for this paper can be obtained by emailing to Lin.Lin@noaa.gov.

References

Aumann, H. H., et al. (2003), AIRS/AMSU/HSB on the Aqua mission: Design, science objectives, data products, and processing systems, *IEEE Trans. Geosci. Remote Sens.*, *41*, 253–264, doi:10.1109/tgrs.2002.808356.

Cao, C., J. Xiong, S. Blonski, Q. Liu, S. Uprety, X. Shao, Y. Bai, and F. Weng (2013), Suomi NPP VIIRS sensor data record verification, validation and long-term performance monitoring, *J. Geophys. Res. Atmos.*, *118*, 11,664–11,678, doi:10.1002/2013JD020418.

Chahine, M. T., et al. (2006), The Atmospheric Infrared Sounder (AIRS): Improving weather forecasting and providing new insights into climate, *Bull. Am. Meteorol. Soc.*, *87*, 911–926, doi:10.1175/BAMS-87-7-911.

Chen, Y., Y. Han, P. van Delst, and F. Weng (2013), Assessment of shortwave infrared sea surface reflection and nonlocal thermodynamic equilibrium effects in the Community Radiative Transfer Model using IASI data, *J. Atmos. Oceanic Technol.*, *30*(9), 2152–2160, doi:10.1175/JTECH-D-12-00267.1.

Chevallier, F., S. D. Michele, and A. P. McNally (2006), Diverse profile datasets from the ECMWF 91-level short-range forecast Rep. NWPSAF-EC-TR-010, 14 pp., Satell. Appl. Facil. for Numer. Weather Predict, Exeter, U. K.

Gambacorta, A., and C. Barnet (2013), Methodology and information content of the NOAA operational channel selection for the Cross-track Infrared Sounder (CrIS), *IEEE Trans. Geosci. Remote Sens.*, *51*(6), doi:10.1109/TGRS.2012.2220369.

Gambacorta, A., C. Barnet, W. Wolf, M. Goldberg, T. King, N. Nalli, E. Maddy, X. Xiong, and M. Divakarla (2012), The NOAA Unique CrIS/ATMS Processing System (NUCAPS): First light retrieval results ITWG meeting, ITWG, Toulouse, France.

Glumb, R., and J. Predina (2002), The Cross-track Infrared Sounder: Sensor design and projected performance The 12th International ATOVS Study Conference (ITSC), Lorne, Victoria, Australia.

Han, Y., F. Weng, Q. Liu, and P. van Delst (2007), A fast radiative transfer model for SSMIS upper atmosphere sounding channels, *J. Geophys. Res.*, *112*, D11121, doi:10.1029/2006JD008208.

Han, Y., et al. (2013), Suomi NPP CrIS measurements, sensor data record algorithm, calibration and validation activities, and record data quality, *J. Geophys. Res. Atmos.*, *118*, 12,734–12,748, doi:10.1002/2013JD020344.

Heidinger, A., and W. C. Straka III (2013), NOAA NESDIS Center for Satellite Applications and Research Algorithm Theoretical Basis Document (ATBD): ABI Cloud Mask, 106 pp.

Kahn, B. H., et al. (2014), The Atmospheric Infrared Sounder version 6 cloud products, *Atmos. Chem. Phys.*, *14*, 399–426, doi:10.5194/acp-14-399-2014.

McNally, A. P., and P. D. Watts (2003), A cloud detection algorithm for High-Spectral-Resolution Infrared Sounders, *Q. J. R. Meteorol. Soc.*, *129*, 3411–3423, doi:10.1256/qj.02.208.

Schreiner, A. J., and T. J. Schmit (2002), Derived cloud products from the GOES-M Imager. Preprints, in *11th Conference on Satellite Meteorology and Oceanography*, pp. 420–423 , American Meteorological Society, Madison, Wis.

Walther, A., and A. K. Heidinger (2013), The expected performance of cloud optical and microphysical properties derived from Suomi NPP VIIRS day/nightband lunar reflectances, *J. Geophys. Res. Atmos.*, *118*, 13,230–13,240, doi:10.1002/2013JD020478.

Weng, F. (2007), Advances in radiative transfer modeling in support of satellite data assimilation, *J. Atmos. Sci.*, *64*, 3799–3807, doi:10.1175/2007JAS2112.1.